Check for updates



ADVANCED MATERIALS TECHNOLOGIES
www.advmattechnol.de

# Reprogrammable 3D Shapes from 1D Metamaterial

*Ezra Ben-Abu,* Anna Zigelman, Yaron Veksler, Sefi Givli, Evgueni Filipov, Hod Lipson, and Amir D. Gat*

**Three billion years of evolution have produced a vast variety of protein molecules, whose functions are directly dependent on their ability to assume and maintain specific shapes. Proteins are defined by the sequence and chemical characteristics of their amino acids, which dictate their 3D shape and function, ranging from enzymatic activity to immune responses. Here, we explore a synthetic form of linear structure that can be bent in a programmable way into various specific 3D shapes inspired by the way functional proteins are defined using genetic codes. This synthetic structure is based on non-circular multistable corrugated tubes, which can be fabricated at various length scales and cross-sectional shapes, thus enabling the modification of their properties. Additionally, the cross-section shape can be rewritten multiple times, allowing for the repair of structural damage and the rewriting of the properties of the structure's multi-stability. A numerical model is used to describe the bending energy landscape of different cross-sections. The proposed reprogrammable 3D shapes of a rewritable 1D metamaterial are promising candidates for futuristic robotic systems, complex deployable structures, catheter devices, and energy absorption and harvesting.**

## 1. Introduction

Reprogramming a specific 3D configuration using 1D structures is crucial for diverse research fields, ranging from biological systems, which rely on protein molecules, to various engineering applications, which utilize metamaterials.[1–4] It is well known that proteins are complex molecules essential to all biological organisms and consist of long chains of amino acids, which are linked together in specific sequences. These sequences determine the unique 3D structure of each protein, which in turn influences its functionality within the body, including enzymatic activity,[5,6] structural support,[7,8] transport and storage,[9,10] cellular signaling,[11–13] immune response[14,15] muscle movement,[16,17] and gene expression regulation.[18,19] The evolution of proteins is a complex process that has taken billions of years.[20] A field of computational protein design aims to automate the design of proteins in a programmable manner,[21–25] thus making this process shorter and more efficient. Extensive research focuses on creating and studying proteins, including X-ray crystallography,[26] nuclear magnetic resonance (NMR) spectroscopy,[27,28] cryo-electron microscopy (Cryo-EM),[29,30] and mass spectrometry.[31,32] There are various physical systems and structures that mimic certain aspects of proteins, often inspired by the unique properties and functions of proteins. These include polymer networks,[33] robotic and mechanical systems,[34] and hydrogels.[35,36]

This functionality has not been replicated in synthetic systems, which are mostly built from continuous 3D parts without the ability to fold into discrete configurations. This limitation restricts the reusability and replicability of structures. The main challenge in overcoming this limitation is the lack of a substrate that would enable comparable performance. Here, we introduce a new substrate, by configuring 1D components into 3D structures through a discrete sequence of operations. This behavior of discrete folding and bending can also be found in multistable structures such as origami structures, e.g., Miura origami[37,38] and Kresling origami,[39–41] and shape-morphing structures.[42,43] The 'Bendy Straw' is another example of a multistable structure, which combines multistability and inflatability, leading to increasing interest in this structure in recent years. For example, Bende et al.,[44] studied experimentally the multistability of the bendy straw that depends on the geometry and internal stress properties in bending and extension states. Later, Ilssar et al.,[45] investigated, both theoretically and experimentally, the dynamic modeling of fluid-filled straw-like elements consisting of serially interconnected elastic frusta with both axisymmetric and antisymmetric degrees

E. Ben-Abu, A. Zigelman, Y. Veksler, S. Givli, A. D. Gat
Faculty of Mechanical Engineering, Technion - Israel Institute of Technology
Haifa 3200003, Israel
E-mail: ezrab@campus.technion.ac.il
E. Filipov
Faculty of Civil and Environmental Engineering
University of Michigan
500 S State St, Ann Arbor, MI 48109, USA
H. Lipson
Faculty of Mechanical Engineering
Columbia University
116th and Broadway, New York 10027, USA

The ORCID identification number(s) for the author(s) of this article can be found under https://doi.org/10.1002/admt.202401113

© 2024 The Author(s). Advanced Materials Technologies published by Wiley-VCH GmbH. This is an open access article under the terms of the Creative Commons Attribution-NonCommercial-NoDerivs License, which permits use and distribution in any medium, provided the original work is properly cited, the use is non-commercial and no modifications or adaptations are made.

**DOI: 10.1002/admt.202401113**

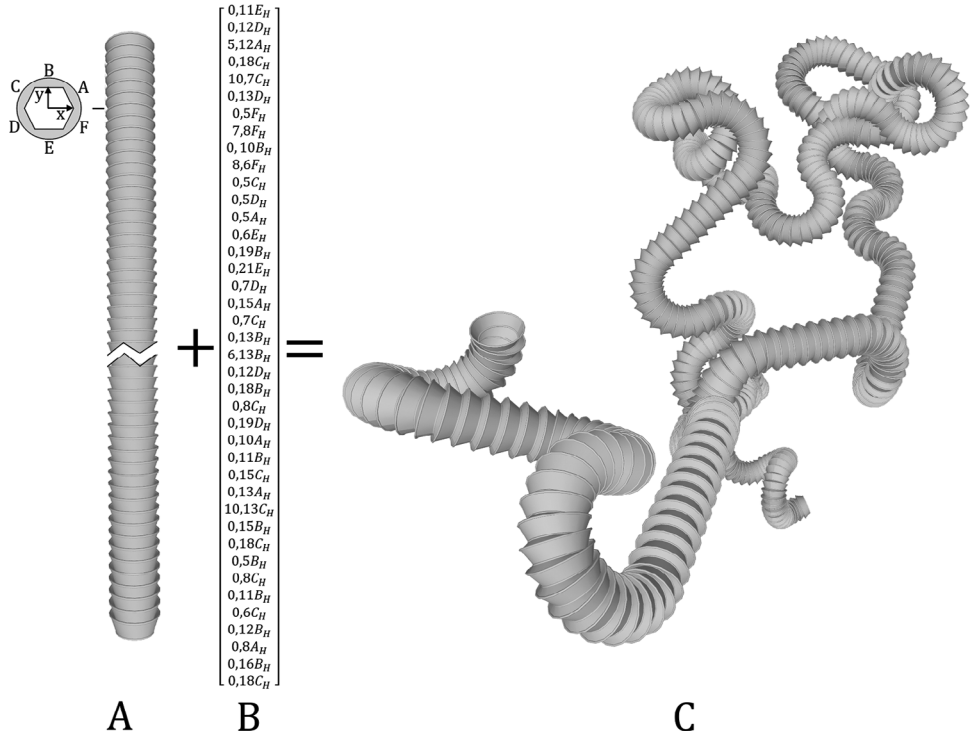



**Figure 1.** Programming complex 3D shapes. A) Given a CFT composed of 500 frusta with a hexagonal (H) cross-section, we impose on it the constraints given as a 2D matrix in B), in order to obtain theoretically the uniquely determined complex 3D configuration shown in C). The number of elongated frusta appears in the first column of each row in (B) and the number of bent frusta with the bend applied at the given point *A*, *B*, *C*, *D*, *E*, or *F* appears in the second column. Note that the number of possible bent points for the hexagonal cross-section is 6.

of freedom. On a different note, Breitman et al.,[46] investigated, both theoretically and experimentally, the fluid-solid-interaction dynamics occurring in a multistable straw filled with a highly viscous fluid. The bending stability of this structure with different cross-sections was studied theoretically by Wo et al.,[47] who used a numerical model based on the bar-and-hinges method. An additional study was proposed by Ben-Abu et al.,[48] who invented a similar structure with helical path, resulting in an additional degree of freedom for twisting, where the non-linear relation between the extension and rotation was examined both experimentally and theoretically. This bendy straw has demonstrated promising characteristics in applications such as soft-growing structures,[49] energy absorption[50] energy harvesting,[51,52] deployable structures,[43] pushing objects,[53] and meta-wire which can be reconfigured rapidly and accurately to arbitrary target shapes.[54]

In this work, we propose 1D metamaterial based on multistable corrugated tubes with programmable and rewritable cross-sections, resulting in a multistable structure with discrete extending, bending, and folding along both the longitudinal and angular axes. To the best of our knowledge, no previous studies have described the manufacturing process for bendy straw, since all of them used pre-manufactured straws. We introduce our fabrication methodology, which is based on controlled and directed mechanical instability, enabling rapid and easy fabrication across multiple length scales. This method allows for the creation of structures with various non-circular shapes, leading to different bending stabilities with preferred directions. Furthermore, the cross-sectional shape of a structure can be altered multiple times without significantly affecting its mechanical properties, which allows for the repair of structural damage and rewriting of its multistable properties, thereby enhancing its durability. The fabrication method is based on a pre-stress process that enables controlled collapse of the tube into a predefined path, yielding a structure with tunable mechanical properties. To analyze the behavior and performance of the bending stability for various cross-sectional shapes of the structure, we used a numerical model developed by Wo et al.[47] With dimensions ranging from centimeters to submillimeters on the radial axis and meters to millimeters on the longitudinal axis, combined with various polymers of the structure, as well as the simplicity and rapidity of the fabrication process, our proposed programmable 3D shapes of a rewritable 1D metamaterial are promising candidates for robotic systems, deployable structures, catheter devices, and energy absorption and harvesting applications.

## 2. Results

Here, we shall discuss the methods that enable us to create the desired and complex 3D configurations based on the corresponding constraints and cross-sectional shapes of the multistable conical frusta tube (hereafter denoted by CFT). In **Figure 1**, we illustrate a complex 3D configuration obtained theoretically, which is composed of 500 bistable elements. Using a similar approach to the theoretical tools presented in our previous paper,[49] we performed a simulation which starts from a closed CFT and a


© 2024 The Author(s). Advanced Materials Technologies published by Wiley-VCH GmbH

2365709x, 2025, 4, Downloaded from https://advanced.onlinelibrary.wiley.com/doi/10.1002/admt.202401113, Wiley Online Library on [30/10/2026]. See the Terms and Conditions (https://onlinelibrary.wiley.com/terms-and-conditions) on Wiley Online Library for rules of use; OA articles are governed by the applicable Creative Commons License

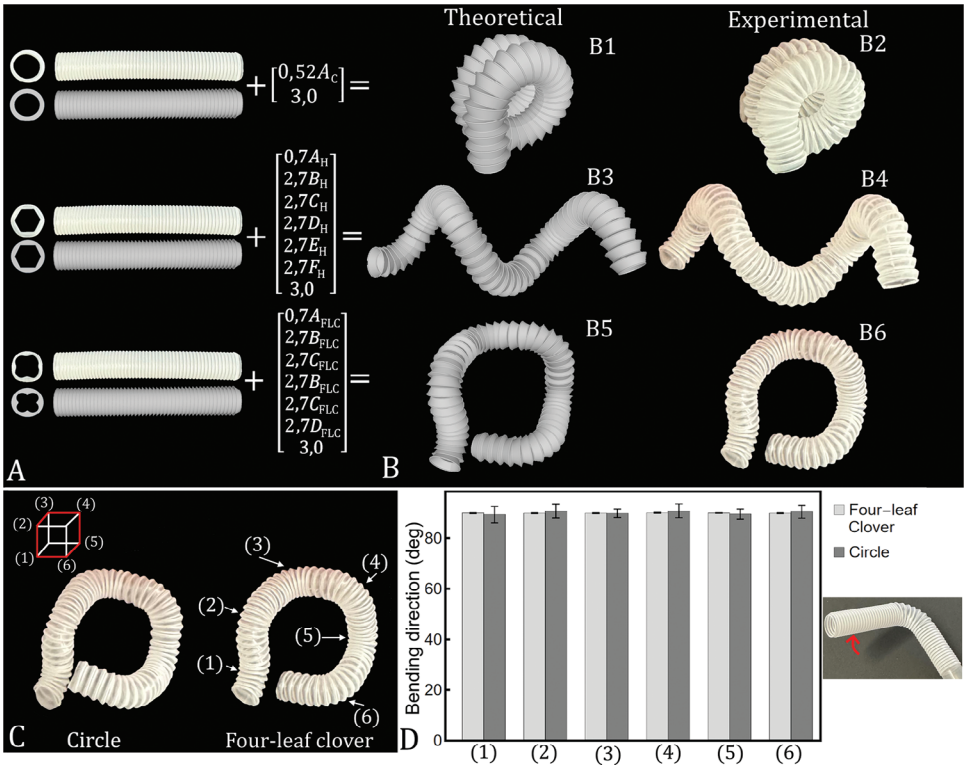



**Figure 2.** Comparison of theoretical and experimental configurations. A) The left column shows pairs of closed CFTs (with circular, hexagonal, and four-leaf clover cross-sections), where the upper CFT in the pair is an image of the CFT in our experiment and the lower CFT is an illustration of the CFT plotted in Phyton. The second column of (A) represents the constraints which are applied on the corresponding CFTs. Note that (3,0) in the constraints vector indicates a "straight section," meaning that three frusta were elongated and zero frusta were bent. B) The theoretical and the experimental results for the CFT configuration subject to the corresponding cross-section and constraints, respectively. C) A demonstration of the importance of the cross-sectional shape of the CFT in achieving a particular 3D configuration: the left and the right columns show the experimental results of bending a CFT with a circular and a four-leaf clover cross-sections, respectively. Although the four-leaf clover cross-section provides a very accurate representation of the red curve shown in the inset (composed of six edges of a cube, where the vertices are indicated by (1)–(6)), the circular cross-section results in a much less accurate approximation of the same curve. D) Comparison between the circular and four-leaf clover cross-sections in terms of the repeatability of the obtained 3D configuration of the CFT. The numbers (1)–(6) on the $x$ −axis represent the corresponding vertex of the cube (as indicated in (C)) and the $y$ −axis shows the bending angle, where the light-grey and grey colors represent the four-leaf clover and the circular cross-sections, respectively. The inset visualizes the definition of the "Bending direction." The error bars were found based on 10 repetitions.

specifically chosen list of constraints (in the matrix form) and yields the desired final 3D configuration. Note that the ability to achieve the particular 3D configurations is due to the angular multistability of the hexagon cross-sectional shape of the CFTs, as will be discussed in Section 2.3.

In **Figure** 2A we show several cross-sectional shapes of the CFTs accompanied with the corresponding lists of constraints (in a matrix form), which is somewhat analogous to the decoding process of protein molecules for different specific 3D configurations. Since, as we show in Section 2.3, preferred bending directions of the CFTs depend on the cross-sectional shape of the CFT, there is a multistability in the angular direction, resulting in 1D structure that has discrete bending and extending states. This allows us to define a vector of constraints that, for each region of the CFT, contains the following information: the number of closed frusta, the cross-sectional shape of the CFT (where we use the notations, H = hexagon, P = pentagon, FLC = four-leaf clover, and TLC = three-leaf clover), the bending point of this cross-section (A, B, C,...), and the number of bent frusta. For example, by the pair ($2,7A_H$) we mean a region which contains in total nine frusta with hexagonal cross-section, two of which are open and seven of which are bent in point A (located at 30°, with respect to the $x$ −axis, as can be seen in Figure 1).

In Figure 2B we show three different 3D configurations of the CFT obtained theoretically and experimentally by using the corresponding cross-sections and constraints, as given in Figure 2A. Note that in order to obtain a helical 3D configuration shown in Figure 2B–B1,B2, we need to use circular cross-section with the angles of $A_C \approx 15.65° \times N$, $N = 1, 2, ..., 23$. Note that is possible to reach these bending angles only in the circular cross-section due to the continuity of the bending directions around the circumference of the circle.

As we shall discuss later, for the hexagonal cross-section, there exist 6 bending points, namely $\{A_H, B_H, C_H, D_H, E_H, F_H\} = \{30°, 90°, 150°, 210°, 270°, 330°\}$, and for the four-leaf clover cross-section, there exist four bending points, namely $\{A_{FLC}, B_{FLC}, C_{FLC}, D_{FLC}\} = \{0°, 90°, 180°, 270°\}$. The two 3D structures shown in Figure 2(B3-B4) and (B5-B6) are only feasible with cross-sections with 6 or 4 angular stability points, respectively, such as in hexagonal or four-leaf clover cross-sections, since these


© 2024 The Author(s). Advanced Materials Technologies published by Wiley-VCH GmbH

2365709x, 2025, 4, Downloaded from https://advanced.onlinelibrary.wiley.com/doi/10.1002/admt.202401113, Wiley Online Library on [30/10/2026]. See the Terms and Conditions (https://onlinelibrary.wiley.com/terms-and-conditions) on Wiley Online Library for rules of use; OA articles are governed by the applicable Creative Commons License

specific angles are required. Note that with the circular cross-section, it is possible to obtain only an approximation of these 3D structures, as it is further visualized in Figure 2C, where we show a comparison between 3D configurations obtained by using a circular and four-leaf clover cross-sections. It can be seen that while a CFT with the four-leaf clover cross-section yields accurately a curve consisting of 6 edges of a cube (shown in the inset of Figure 2C), the CFT with the circular cross-section results only in a rough approximation of the same curve. In Figure 2D, we show a bar chart of the bending direction as a function of the location along the curve, with the numbers (1)–(6) representing the six vertices of the cube. The light grey and grey colors correspond to the four-leaf clover and circular cross-sections, respectively. The error bar lengths highlight the repeatability of the 3D structure with the CFT four-leaf clover cross-section, compared to the lack of repeatability with the circular cross-section. Note that 90° is the reference angle of the "Bending direction" in Figure 2D as can be seen in the inset, for the case in which the two "straight" center lines between the bent parts are perpendicular to each other and located on the same plane. In the case of the four-leaf clover, we have four stable bending directions, and when we bend the structure, the "straight" center lines remain always on the same plane, as expected and measured. For the circular cross-section, however, the structure can be rotated about the angular axis, and we measured the angle between the two planes containing the center lines of two bent sections of the bendy straw, which is a bit less than 10°. The angle between the planes was added or subtracted based on the direction of the plane of the current bendy straw section relative to the plane of the previous section.

### 2.1. Fabrication Methods

Here we shall discuss the fabrication process, the repairing procedure, and the rewriting ability of our proposed multi-stable non-circular structure composed of interconnected multiple bi-stable frusta. It is known that the bi-stability of a frustum in a multi-stable structure is achieved through a thin-thick-thin thickness pattern of the material, see e.g., Qiu et al.[55] our methodology, this thickness pattern is achieved by the pre-stress process, which creates plastic deformations along the longitude direction. A CFT is fabricated as follows. First pre-stress lines on an elastic tube are created. This is achieved by inserting a circular engraving mandrel (with the desired geometric parameters) into the elastic tube (see **Figure** 3A–A1) and applying the external force (see Figure 3A–A2). This force causes plastic deformation on the unsupported grooves along the mandrel. In the second stage, we create a buckling pattern along the elastic tube by applying compression forces on the elastic tube (see Figure 3A–A3) and thus the desired CFT (see Figure 3A–A4) is fabricated via a mechanism of elastic instability. The entire fabrication process of a CFT lasts in average ≈1 min (see Movie S1, Supporting Information).

In Figure 3B, we show four different cross-sections of the CFT which we fabricated in the experiment. Specifically, the CFTs with the cross-sections of a circle, a pentagon, a three-leaf clover, and a five-leaf clover are shown in Figure 3B–B1–B4, respectively. In Figure 3C, we emphasize the simplicity of the repairing procedure, which may take place even after multiple instances of damage. This process comprises of the following two steps: 1) inserting a buckling mandrel (see Figure 3C–C3) and 2) buckling the structure several times to repair it (see Figure 3C–C4). Moreover, note that our multistable structure may be produced in a wide range of dimensions. To emphasize this, we show in Figure 3D, multiple length scales of CFT both in the radial direction, spanning from centimeter scale down to sub-millimeter scale, and in the axial direction, spanning from meter scale down to millimeter scale. To highlight the difference in length scales even more, the smallest CFT that we fabricated and a large CFT which is commercially available, are shown in Figure 3E.

### 2.2. Mechanical Properties

The mechanical properties of a CFT include geometrical properties such as the lumen ratio (a ratio between the inner and outer radii), the bending angle, and the elongation, as well as the material properties. The material properties which we examine in the current study are the threshold pressure, which determines the structure's stiffness, and the bending stability. In our case, the threshold pressure refers to the pressure at which snap-through occur. Note that for the circular case the bending stability is homogeneous along the radial axis and for non-circular cross-sections it has preferred directions.

In **Figure** 4 we show four panels corresponding to four different frustum static heights $h_2 \in \{1.5, 1.75, 2, 2.25\}$ mm, where in each panel the experimentally measured threshold pressure is plotted versus the frustum width, $w \in \{0.5, 0.75, 1, 1.25\}$ mm. For all panels, each line in the panel interpolates the experimental results measured for four different frustum dynamic heights $h_1 \in \{0.5, 0.75, 1, 1.25\}$ mm (each experiment repeated three times on different CFTs), where the lowest line represents the smallest value of $h_1$, increasing as the lines move upwards. In total, we have fabricated 192 CFTs for this figure, where in all cases, during the fabrication process we applied the same force in ambient temperature to ensure that the threshold pressure of all CFTs will be dictated only by the geometric properties of the CFT. In all measurements, the standard deviation of the threshold pressure measurements is below 0.036 atm.

It can be seen in Figure 4 that the range of the threshold pressure that we measured is from 0.52 to 2.05 atm. Moreover according to the figure, the threshold pressure increases approximately linearly with the geometric parameters ($h_1$, $h_2$, and $w$).

### 2.3. Different Cross-Sections and Rewritable Properties

We will first discuss the importance of different cross-sections of the CFT. Note that when a circular CFT is bent, it does not possess strong resistance to rotation around the radial axis due to the homogeneous bending stability. However, the ability to control the bending stability and its preferred directions are crucial for precise maneuvers in various applications, such as robotic arms and growing robots.[49,56,57] More specifically, by using a non-cylindrical (e.g., hexagonal) buckling mandrel, we can increase the rotational resistance by creating preferred bending directions, thus providing a stiffer structure which is more suitable for these applications. For example, a CFT with hexagonal cross-section possesses 6 preferred bending directions, where due to


© 2024 The Author(s). Advanced Materials Technologies published by Wiley-VCH GmbH

2365709x, 2025, 4, Downloaded from https://advanced.onlinelibrary.wiley.com/doi/10.1002/admt.202401113, Wiley Online Library on [30/10/2026]. See the Terms and Conditions (https://onlinelibrary.wiley.com/terms-and-conditions) on Wiley Online Library for rules of use; OA articles are governed by the applicable Creative Commons License

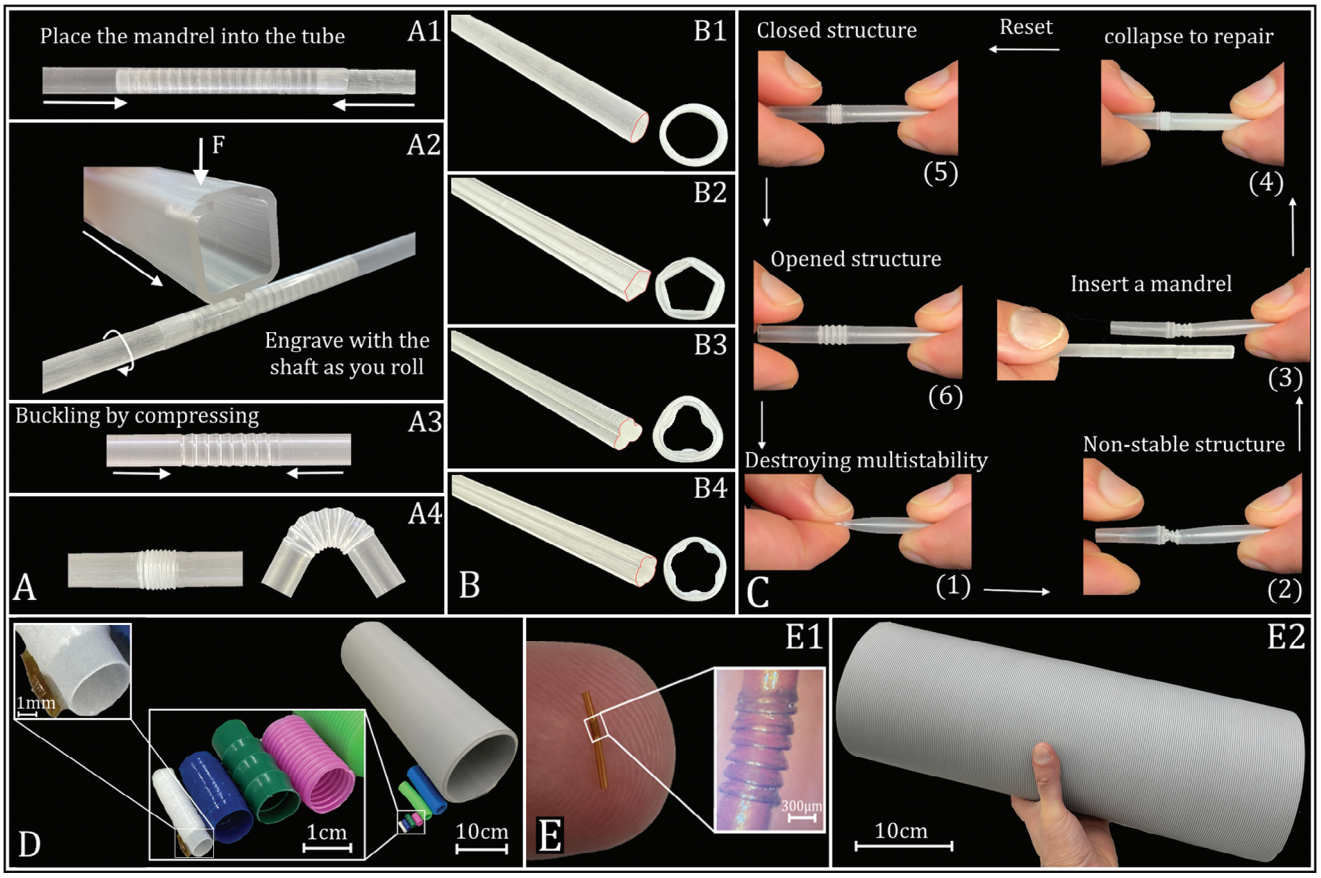



**Figure 3.** Fabrication and repairing process of CFT. A) The production process of the multi-stable CFT which consists of four steps: (A1) placing the elastic tube on the mandrel, (A2) engraving with the engraving shaft to achieve the pre-stressed pattern, (A3) replacing the engraving mandrel with a buckling mandrel and compressing the elastic tube with axial forces, and (A4) obtaining the desirable multi-stable CFT. B) Different cross-sections of the CFT including a circle, a pentagon, a three-leaf clover, and a five-leaf clover, along with their corresponding buckling mandrels. C) The repairing process starts after the multistability was destroyed (1) and the resulting CFT became unstable (2). This process contains two steps: placing the mandrel into the tube (3) and buckling by compressing the structure (4). This yields a CFT which is multistable again, whose closed and open states are shown in (5) and (6), respectively. This loop of destroying and repairing the multistable structure can be repeated multiple times. D) An isometric comparison of circular CFTs made of different materials and with varying sizes. Each inset corresponds to a magnification by an order of magnitude, highlighting the size difference. E) The range of CFTs: (E1) the smallest CFT that we fabricated, with an enlarged view, where a human finger provides a scale reference, and (E2) a large CFT which is commercially available. The scale bars correspond to 10 cm, 10 mm, 1 mm, and 300 μm.

non-homogeneous energy landscape, one needs to invest energy in order to switch from one preferred bending direction to the next one.

In **Figure** 5A, we show six different cross-sections: circle, hexagon, pentagon, three-leaf clover, four-leaf clover, and five-leaf clover, along with their corresponding bending energy landscapes. The bending energy landscapes were found by using a numerical code, based on the bar-and-hinges model of Wo et al.,[47] where the details of the polar expressions for the circumferences of the various cross-sections are given in Supporting Information. Note that the non-dimensional energy was obtained according to the transformation $\bar{E} = E/(kt^3)$, where $\bar{E}$, $E$, $k$, and $t$ denote the non-dimensional energy, the total dimensional energy (including folding, bending, and stretching energy from the bar-and-hinges model), the stiffness, and the thickness of the structure, respectively. The range of the bending angles in Figure 5A varies from 0 at the center of the structure till a maximum value of ≈12° at the boundary of the bending energy landscapes. The stars in the figure represent the locations of the lowest local minima of the bending stability and visualize the fact that in all of the examined cases, except the circle, there are several discrete preferred directions along which the CFT can be bent. If one wishes to switch from one preferred direction (indicated by a star) to the neighboring direction, energy must be invested in order to overcome the energy barrier that separates the two equilibrium configurations. Note that different paths, that connect the two preferred directions, may cross the barrier at locations that are characterized by different crossing (barrier) energy. Here, different paths refer to different trajectories in the curvature-orientation space (radial-tangential directions in the polar plot of the energy). The minimum barrier corresponds to a saddle point of the energy landscape, which is an unstable equilibrium configuration. Interestingly, the minimum-barrier trajectory (the path that crosses the barrier at the saddle point) must involve changing the curvature of the CFT (the radius in the radial plot) together with the orientation. Generally, it can be seen that as


© 2024 The Author(s). Advanced Materials Technologies published by Wiley-VCH GmbH

2365709x, 2025, 4, Downloaded from https://advanced.onlinelibrary.wiley.com/doi/10.1002/admt.202401113, Wiley Online Library on [30/10/2026]. See the Terms and Conditions (https://onlinelibrary.wiley.com/terms-and-conditions) on Wiley Online Library for rules of use; OA articles are governed by the applicable Creative Commons License

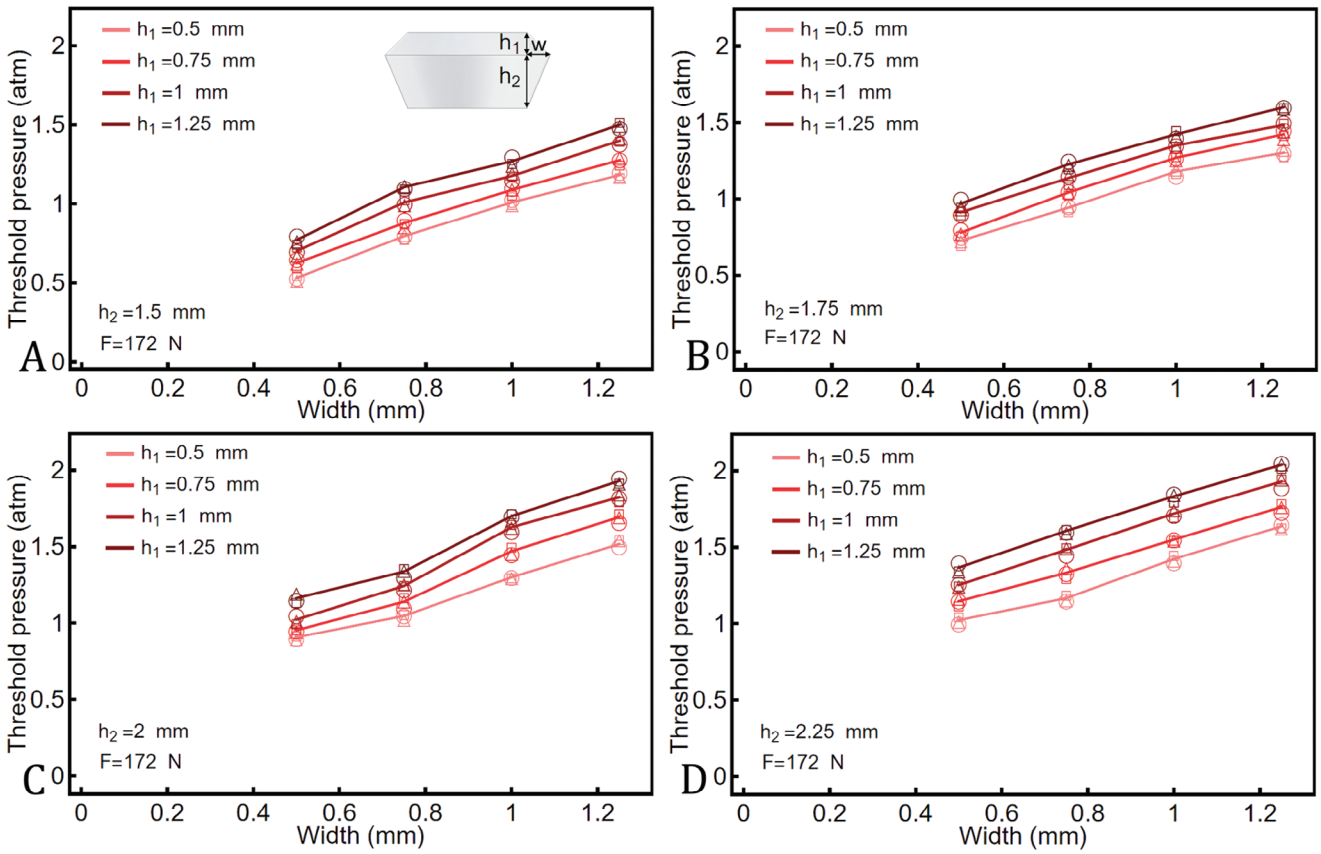



**Figure 4.** Experimental measurements of the stability thresholds for different ratios between the (width/heights) dimensions of the circular frustum. Experimental measurements of the threshold pressure (in atm) vs the width of the frustum (in mm) are denoted by red circles, squares, and triangles (which denote three repetitions of each experiment, using different CFTs). Each line represents a different dynamic height $h_1$ (in mm), with the lowest line representing the smallest value of $h_1$, increasing as the lines move upwards. The panels correspond to different static heights as follows: A) $h_2$ = 1.5 mm, B) $h_2$ = 1.75 mm, C) $h_2$ = 2 mm, and D) $h_2$ = 2.25 mm. The top-right part of panel (A) is an illustration of our notations. All experiments were conducted with the same force of 172 N.

the number of stars decreases, more energy is needed in order to switch between preferred bending directions. This cannot be seen in the case of the three-leaf clover, because this simulation was performed with a different set of parameters, due to the numerical restrictions. An additional observation is obtained when comparing Figure 5A–A4,A6, a pentagon and a five-leaf clover, both having 5 stars in their energy landscapes. It can seen, that when the edges of the cross-section are straight, it is more difficult to switch from one preferred direction to the next one, than in case that the edges of the cross-section are curved. In the second part of Movie S1 (Supporting Information), it can be seen that for the pentagon sufficient force is needed to be applied in order to transit between one preferred bending direction to another.

Due to the different energy landscapes of the various cross-sections, it may be advantageous to be able to reshape the CFT in an easy and fast process even after the initial fabrication process. In Figure 5B, we demonstrate the rewriting process of one cycle in our experiment, where each cycle consists of three transitions: 1) from a circle to a pentagon, 2) from a pentagon to a four-leaf clover, and 3) from a four-leaf clover to the circle. In each reshaping stage, the CFT is buckled several times on the corresponding buckling mandrel, until it obtains the desired cross-section with multistability in the longitude direction. An entire cycle takes ≈1 min, making this concept user-friendly.

An additional aspect of reshaping a CFT is its durability as a multistable structure, even after multiple rewriting cycles. In Figure 5C, we show two bar charts. The top chart shows the threshold pressures for a circle, a pentagon, and a four-leaf clover for 50 cycles, each containing 3 rewriting stages (as shown in Figure 5B) and thus resulting in 150 rewriting stages. As it can be easily observed by looking at the error bars, the number of cycles has no significant effects on the resulting mechanical properties and the difference between the smallest and the largest threshold pressure values for all of the cross-sections examined was ≈5 percent. The bottom bar chart displays the bending angle for all angularly stable configurations of the pentagonal cross-section. The angle in all stable states was measured 10 times and the median angular error was found to be only ≈0.3°.

In **Figure 6**, we show the threshold pressure and the relative thickness versus the applied force during the fabrication process for various cross-sections, sizes, and materials of the CFT, where in all cases the geometric parameters of the engraving mandrel were $h_1 = w = 0.75$ mm and $h_2 = 1.75$ mm. For the measurements shown in Figure 6A,C we used different materials and


© 2024 The Author(s). Advanced Materials Technologies published by Wiley-VCH GmbH

2365709x, 2025, 4, Downloaded from https://advanced.onlinelibrary.wiley.com/doi/10.1002/admt.202401113, Wiley Online Library on [30/10/2026]. See the Terms and Conditions (https://onlinelibrary.wiley.com/terms-and-conditions) on Wiley Online Library for rules of use; OA articles are governed by the applicable Creative Commons License

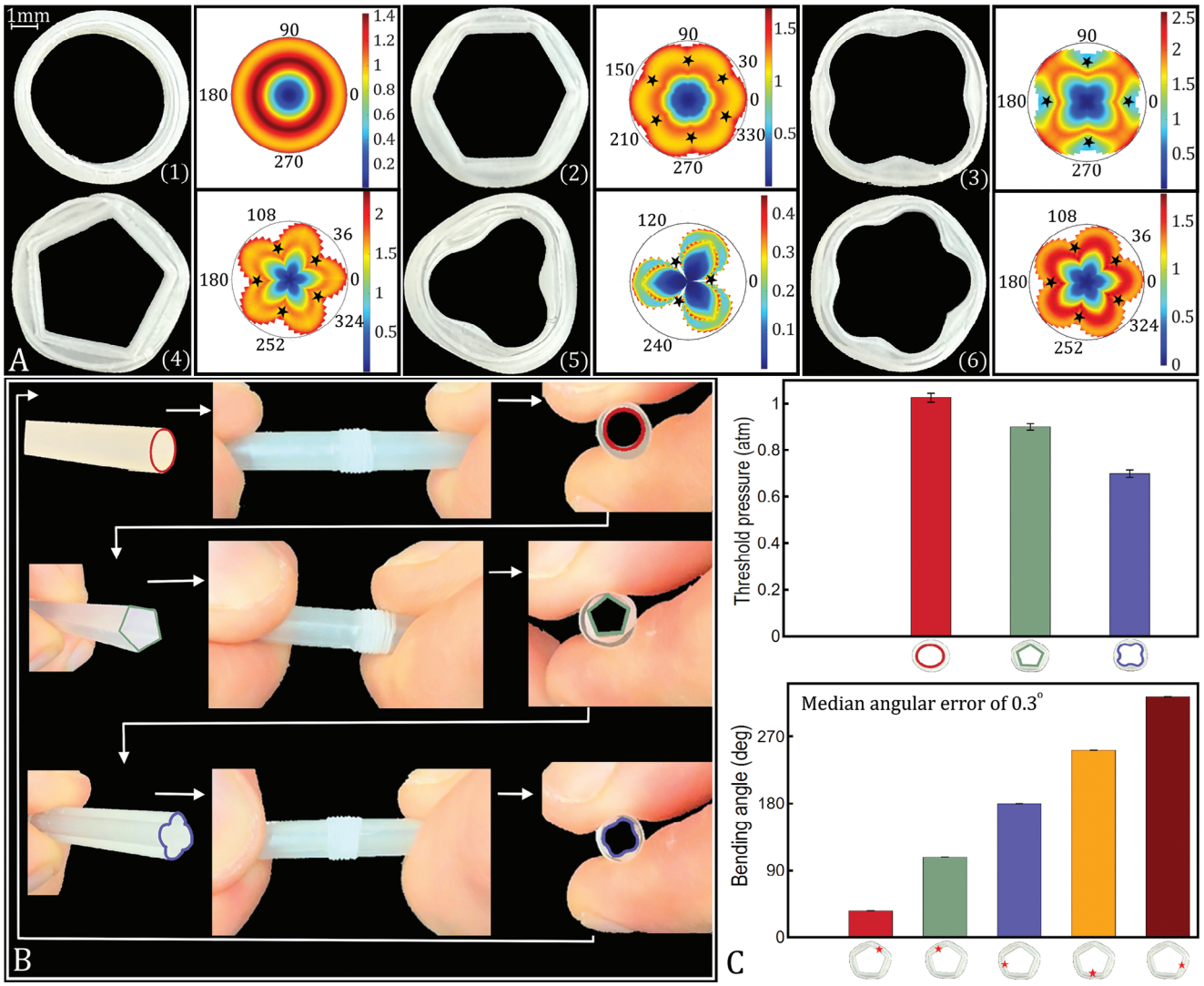



**Figure 5.** Rewritable CFTs with different cross-sections: A) Different cross-section CFTs that we fabricated in experiment and their energy landscapes obtained by simulation using the MERLIN2 software.[47] In the energy landscapes, the colorbars represent the dimensionless energy, emphasizing the preferred bending directions. Except for the three-leaf clover in panel (A5) (which has more severe numerical restrictions), all energy calculations were carried out using the same parameters. The energy is plotted versus the bending angle in polar coordinates, where the stars represent the lowest local minima in the bent state. B) Demonstration of one cycle in our experiment, where each cycle consists of three transitions: 1) from a circle to a pentagon, 2) from a pentagon to a four-leaf clover, and 3) from a four-leaf clover to the circle. C) Two bar charts representing the structural repeatability. The top chart shows the pressure threshold (in atm) for three different cross-sections (circle, pentagon, and four-leaf clover) over 50 cycles, with error bars. Red, green, and blue colors correspond to the pressures measured for a circle, a pentagon, and a four-leaf clover, respectively. On the bottom chart, the bending angle for all angularly stable configurations of the pentagonal cross-section is displayed. The scale bar in panel (A) corresponds to 1 mm and the error bars in the bottom chart in (C) have median angular error of 0.3°.

diameters of the CFTs, including: Nylon (with the diameter of 8 mm), Polypropylene (with the diameters of 8, 6, and 4 mm), and Pebax (with the diameter of 6 mm). For the measurements shown in Figure 6B,D we used different cross-sections of the CFTs, including: a circle, a hexagon, a pentagon, a three-leaf clover, a four-leaf clover, and a five-leaf clover. As can be seen in Figure 6A,B, in all cases there exists a local maximum in the threshold pressure, which is attained for the force in the range between 150 N and 200 N, whereas according to Figure 6C,D the relative thickness of the CFT monotonically decreases as a function of the applied force. The local maximum in the threshold pressure can be explained as follows. Initially, as we increase the force, we continuously modify the geometry of the CFT to be frusta-like until it accepts the shape of the engraving mandrel. In this stage the threshold pressure monotonically increases. After the CFT reached the shape of the engraving mandrel, continuing to increase the force will create significant thinning of the material, weakening the structure as evident in the insets in Figure 6C, and thus resulting in the threshold pressure reduction. Moreover, as it can be observed in Figure 6C,D, the relative thickness of the CFT depends on its material and diameter, but it is independent of its cross-section.


© 2024 The Author(s). Advanced Materials Technologies published by Wiley-VCH GmbH

2365709x, 2025, 4, Downloaded from https://advanced.onlinelibrary.wiley.com/doi/10.1002/admt.202401113, Wiley Online Library on [30/10/2026]. See the Terms and Conditions (https://onlinelibrary.wiley.com/terms-and-conditions) on Wiley Online Library for rules of use; OA articles are governed by the applicable Creative Commons License

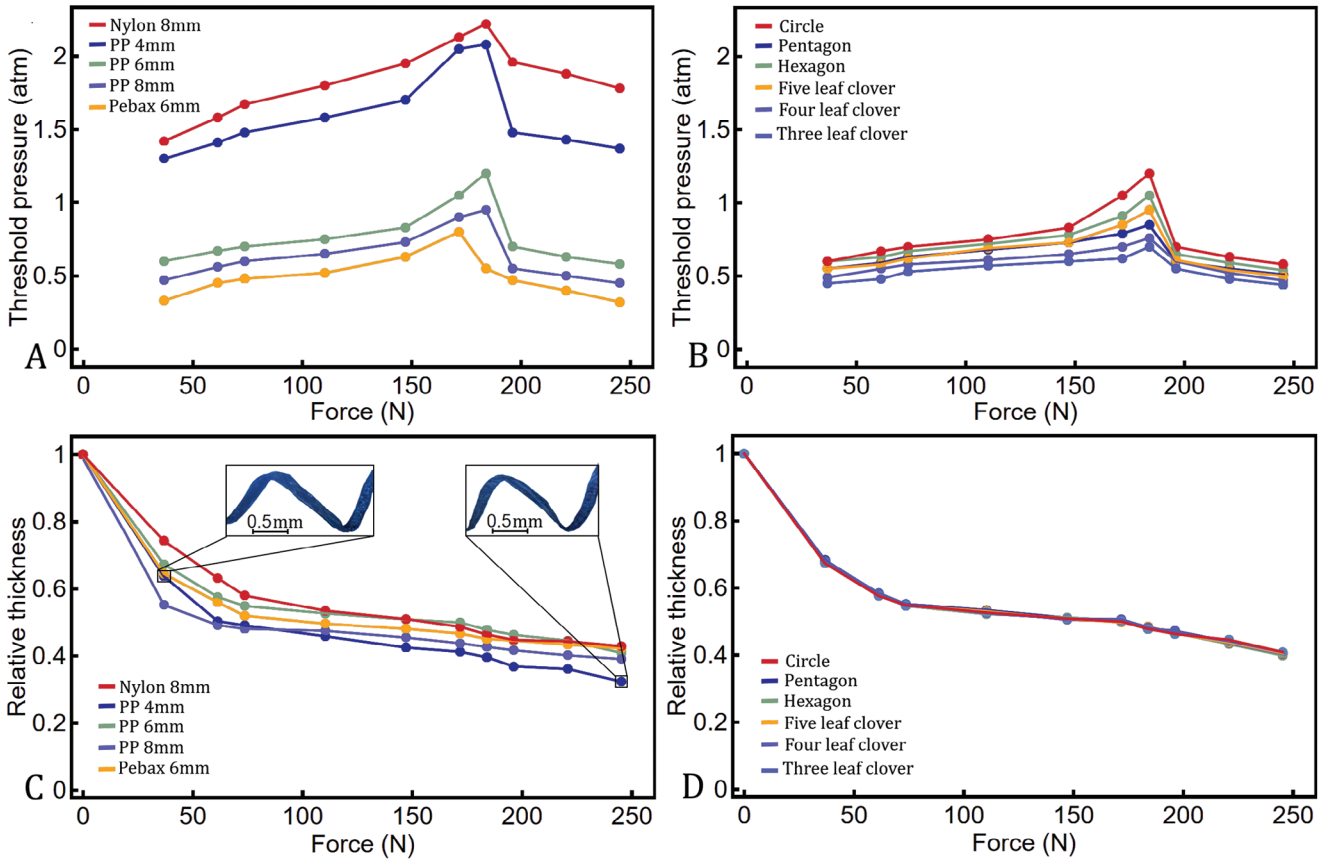



**Figure 6.** Experimental measurements of the stability threshold and the relative thickness versus the applied force for different materials and cross-sections. Experimental measurements of the threshold pressure (in atm) versus the force applied in the fabrication process (in N) for A) different materials and tubes' diameter, as labeled in the figure, and B) different cross-sections, as labeled in the figure. Experimental measurements of the relative thickness (the thinnest thickness is divided by the natural thickness) versus the force applied in the fabrication process (in N) for C) different materials and tubes' diameter, as labeled in the figure, and D) for different cross-sections, as labeled in the figure. An enlarged view of the axial cross-section of the frustum boundary is shown in insets in panel (C). The scale bars correspond to 0.5 mm.

## 3. Concluding Remarks

In this study we present a programmable structure that is multistable in both angular and axial directions, resulting in a structure capable of achieving specific 3D configurations. In order to fabricate this unique structure, we propose a novel fabrication method, which is rapid, simple, and cost-effective, that enables us to obtain multistable CFTs with circular or non-circular frusta. Note, that our methodology allows to specify longitudinal extension and radial bending in discrete "digital" steps that can be specified by a sequence of symbols. Moreover, as long as the external forces which are applied during the pre-stress process remain the same, the process is repeatable with 0.08% error. The same fabrication process remains valid for a variety of materials, cross-sectional shapes, tubes' walls thicknesses, and radii, thus spanning a wide range of material and geometrical properties.

Indeed, the effect of the cross-sectional shape of the CFT on its multistable properties is drastic. To emphasize this variety, we have performed numerical simulations that yielded bending energy landscapes for different shapes, revealing distinct preferred directions of bending stability. Thus, a cross-sectional shape of the CFT can be selected in advance, as dictated by the specific aims of the application. Moreover, the angular stability of the cross-sectional shape of the CFT allows to get a uniquely determined complex 3D configuration in analogy to protein molecules. The cross-sectional shapes and constraints dictating the resulting 3D configuration may be determined in advance.

After the CFT is fabricated, it can be rewritten multiple times, in terms of transferring one cross-sectional shape to another, where the mechanical properties of the CFT depend only on its current cross-sectional shape without taking into account the history of the transformations. The validity of this capability was demonstrated by reshaping the cross-sectional shape 150 times, where the threshold pressure for specific cross-sectional shapes was approximately not affected by the number of transformations during the rewriting process. Furthermore, according to our verification, the fabricated CFT can endure thousands of loading cycles without malfunction and by following the same methodology as the rewriting procedure, the structure can be easily repaired multiple times if damaged, which enables to restore its multistable properties. All of the above implies that the proposed rewritable multistable CFTs offer a promising improvement for controlling the bending stability of the structure, with the ability to rewrite and tune it as needed. The fabrication method


© 2024 The Author(s). Advanced Materials Technologies published by Wiley-VCH GmbH

2365709x, 2025, 4, Downloaded from https://advanced.onlinelibrary.wiley.com/doi/10.1002/admt.202401113, Wiley Online Library on [30/10/2026]. See the Terms and Conditions (https://onlinelibrary.wiley.com/terms-and-conditions) on Wiley Online Library for rules of use; OA articles are governed by the applicable Creative Commons License

proposed in this study for the first time enables the use of versatile multistable structures, relevant for applications such as medical devices (e.g., catheters) and robotic actuation mechanisms, in which multistable properties are written onto the structure as needed and can be rewritten or repaired at any moment according to the demand.

## 4. Experimental Section

In this study, a fabrication method for a synthetic form of a linear structure that can be bent in a programmable way is proposed. This synthetic structure was based on multistable non-circular CFTs with rewritable properties. CFTs were fabricated from a variety of materials with differing geometries and cross-sections using the appropriate mandrels and engraving shafts. Moreover, it was shown that the CFT can be fabricated in multiscale dimensions.

*Fabrication of Non-Circular Frusta and the Experimental Setup*: All of the mandrels used in this study were printed by using SLA 3D printer (Form 3B+). Moreover, the CFTs shown in Figures 4 and 5 were made of 6 mm Polypropylene tubes ($E = 1.3$ GPa). Note that the CFTs were fabricated with four different dynamic heights and depths of $h_1$, $w \in \{0.5, 0.75, 1, 1.25\}$ mm, as well as four different static heights of $h_2 \in \{1.5, 1.75, 2, 2.25\}$ mm. The number of the bistable elements in each CFT was in the range of 3–25 elements. In all experiments, the CFT was directly connected with an elastic tube to a pressure controller (ELVEFLOW OB1 MK3+), which in turn was connected to a compressor (CompAir L07). In all experiments, the pressure controller was adjusted to $[0.33, 2.1] \pm 0.01$ atm and the temperature was kept at room temperature. The other side of the CFT was sealed with hot glue. All videos were captured in 4K resolution and 60 frames per second. The bending direction angle in Figure 2D was measured with an analog protractor, with an accuracy of 0.1°. The protractor was always placed perpendicular to the plane containing the "straight" center line of the previous section of the bendy straw, and parallel to the plane containing the "straight" center line of the current section of the bendy straw. All panels of Figures 3, 4, and 5 were captured with IPhone 15pro max camera, whereas the increased view in panel (E1) of Figure 3 was captured with a digital microscope (LCD ATFWEL).

The CFTs shown in Figures 3 and 6 were made from Polypropylene, Polyolefin, and medical grade polymers: Polyimide, Nylon Grilamid, and Pebax 7233. The tubes' walls thicknesses ranged from 250 to 20 µm and the range of their inner radii was from 7.5 cm to 292 µm.

## Supporting Information

Supporting Information is available from the Wiley Online Library or from the author.

## Acknowledgements

E.B.A. is grateful to the Azrieli Foundation for the award of an Azrieli Fellowship.

## Conflict of Interest

The authors declare no conflict of interest.

## Author Contributions

A.D.G., H.L., and E.B.A. conceived the research subject. E.B.A. constructed the experimental setup and conducted the experiments. Y.V. prepared the theoretical figures of the various 3D CFTs' configurations. E.F. provided the numerical algorithm for the computation of the energy landscapes and guided A.Z. and E.B.A. to employ it for the examples shown in the paper. A.Z. and E.B.A. generated the energy landscapes graphs using this algorithm. E.B.A. analyzed the experimental data. E.B.A., A.Z., S.G., H.L., and A.D.G. wrote the paper.

## Data Availability Statement

The data that support the findings of this study are available from the corresponding author upon reasonable request.

## Keywords

mechanical properties, metamaterials, multistable structures, reprogrammable 3D shapes, rewritable shapes

Received: July 11, 2024
Revised: September 16, 2024
Published online: October 9, 2024

[1] V. Zykov, E. Mytilinaios, B. Adams, H. Lipson, *Nature* **2005**, *435*, 163.
[2] N. Gershenfeld, *Foreign Aff.* **2012**, *91*, 43.
[3] N. Gershenfeld, M. Carney, B. Jenett, S. Calisch, S. Wilson, *Archit. Des.* **2015**, *85*, 122.
[4] B. Jenett, C. Cameron, F. Tourlomousis, A. P. Rubio, M. Ochalek, N. Gershenfeld, *Sci. Adv.* **2020**, *6*, eabc9943.
[5] P. Forrer, S. Jung, A. Plückthun, *Curr. Opin. Struct. Biol.* **1999**, *9*, 514.
[6] M. Vendruscolo, *Curr. Opin. Chem. Biol.* **2010**, *14*, 671.
[7] J. J. Burbaum, R. M. Starzyk, P. Schimmel, *Proteins* **1990**, *7*, 99.
[8] M. K. Gardner, J. Haase, K. Mythreye, J. N. Molk, M. Anderson, A. P. Joglekar, E. T. O'Toole, M. Winey, E. Salmon, D. J. Odde, K. Bloom, *J. Cell Biol.* **2008**, *180*, 91.
[9] P. Aisen, I. Listowsky, *Annu. Rev. Biochem.* **1980**, *49*, 357.
[10] R. Blomhoff, M. H. Green, T. Berg, K. R. Norum, *Science* **1990**, *250*, 399.
[11] T. R. Soderling, B. Chang, D. Brickey, *J. Biol. Chem.* **2001**, *276*, 3719.
[12] J. Westermarck, J. Ivaska, G. L. Corthals, *Mol. Cell. Proteomics* **2013**, *12*, 1752.
[13] R. M. Gordley, L. J. Bugaj, W. A. Lim, *Curr. Opin. Struct. Biol.* **2016**, *39*, 106.
[14] S. H. Kaufmann, *Immunol. Today* **1990**, *11*, 129.
[15] P. Moseley, *Immunopharmacology* **2000**, *48*, 299.
[16] K. C. Holmes, *Curr. Opin. Struct. Biol.* **1996**, *6*, 781.
[17] R. D. Vale, R. A. Milligan, *Science* **2000**, *288*, 88.
[18] M. F. Wilkinson, A.-B. Shyu, *Bioessays* **2001**, *23*, 775.
[19] P. R. Manna, M. T. Dyson, D. M. Stocco, *Mol. Hum. Reprod.* **2009**, *15*, 321.
[20] *The UniProt Consortium, Nucleic Acids Research* **2021**, *49*, D480.
[21] J. M. Smith, *Nature* **1970**, *225*, 563.
[22] N. Koga, R. Tatsumi-Koga, G. Liu, R. Xiao, T. B. Acton, G. T. Montelione, D. Baker, *Nature* **2012**, *491*, 222.
[23] N. H. Joh, T. Wang, M. P. Bhate, R. Acharya, Y. Wu, M. Grabe, M. Hong, G. Grigoryan, W. F. DeGrado, *Science* **2014**, *346*, 1520.
[24] P.-S. Huang, S. E. Boyken, D. Baker, *Nature* **2016**, *537*, 320.
[25] J. B. Ingraham, M. Baranov, Z. Costello, K. W. Barber, W. Wang, A. Ismail, V. Frappier, D. M. Lord, C. Ng-Thow-Hing, E. R. Van Vlack, S. Tie, V. Xue, S. C. Cowles, A. Leung, J. V. Rodrigues, C. L. Morales-Perez, A. M. Ayoub, R. Green, K. Puentes, F. Oplinger, N. V. Panwar, F. Obermeyer, A. R. Root, A. L. Beam, G. Grigoryan, *Nature* **2023**, *623*, 1070.


© 2024 The Author(s). Advanced Materials Technologies published by Wiley-VCH GmbH

2365709x, 2025, 4, Downloaded from https://advanced.onlinelibrary.wiley.com/doi/10.1002/admt.202401113, Wiley Online Library on [30/10/2026]. See the Terms and Conditions (https://onlinelibrary.wiley.com/terms-and-conditions) on Wiley Online Library for rules of use; OA articles are governed by the applicable Creative Commons License

[26] J. Drenth, *Principles of Protein X-ray Crystallography*, Springer Science & Business Media, Berlin, Germany **2007**.
[27] F. A. Bovey, P. A. Mirau, H. Gutowsky, *Nuclear Magnetic Resonance Spectroscopy*, Elsevier, Amsterdam, Netherlands **1988**.
[28] K. Wüthrich, *ENCYCLOPEDIA OF LIFE SCIENCES* **2001**.
[29] N. Thonghin, V. Kargas, J. Clews, R. C. Ford, *Methods* **2018**, *147*, 176.
[30] M. Bonomi, M. Vendruscolo, *Curr. Opin. Struct. Biol.* **2019**, *56*, 37.
[31] M. Mann, R. C. Hendrickson, A. Pandey, *Annu. Rev. Biochem.* **2001**, *70*, 437.
[32] B. Domon, R. Aebersold, *Science* **2006**, *312*, 212.
[33] M. Jaspers, S. L. Vaessen, P. van Schayik, D. Voerman, A. E. Rowan, P. H. Kouwer, *Nat. Commun.* **2017**, *8*, 15478.
[34] H. Jia, J. Flommersfeld, M. Heymann, S. K. Vogel, H. G. Franquelim, D. B. Brückner, H. Eto, C. P. Broedersz, P. Schwille, *Nat. Mater.* **2022**, *21*, 703.
[35] H. Geckil, F. Xu, X. Zhang, S. Moon, U. Demirci, *Nanomedicine* **2010**, *5*, 469.
[36] J. Wu, P. Li, C. Dong, H. Jiang, B. Xue, X. Gao, M. Qin, W. Wang, B. Chen, Y. Cao, *Nat. Commun.* **2018**, *9*, 620.
[37] K. Miura, M. Natori, *Space Sol. Power Rev.* **1985**, *5*, 345.
[38] K. Miura, *Int. J. Space Struct.* **1993**, *8*, 3.
[39] S. D. Guest, S. Pellegrino, *J. Appl. Mech.* **1994**, *61*, 773.
[40] S. D. Guest, S. Pellegrino, *J. Appl. Mech.* **1994**, *61*, 778.
[41] S. D. Guest, S. Pellegrino, *J. Appl. Mech.* **1996**, *63*, 77.
[42] A. S. Meeussen, M. van Hecke, *Nature* **2023**, *621*, 516.
[43] Y. Veksler, E. Ben-Abu, A. D. Gat, *Adv. Intell. Syst.* **2024**, *6*, 2400179.
[44] N. P. Bende, T. Yu, N. A. Corbin, M. A. Dias, C. D. Santangelo, J. A. Hanna, R. C. Hayward, *Soft Matter* **2018**, *14*, 8636.
[45] D. Ilssar, M. Pukshansky, Y. Or, A. D. Gat, *Phys. Rev. Appl.* **2022**, *18*, 034041.
[46] P. Breitman, M. Pukshansky, A. Zigelman, E. Ben Abu, O. Peretz, S. Givli, A. D. Gat, *Phys. Rev. Appl.* **2022**, *18*, 064077.
[47] Z. Wo, E. T. Filipov, *J. Appl. Mech.* **2022**, *89*, 041005.
[48] E. Ben-Abu, Y. Abramov, A. Fine, S. Elbaz, N. Zemah, A. Zigelman, O. Ram, A. D. Gat, *Adv. Eng. Mater.* **2024**, *26*, 2400070.
[49] E. Ben Abu, Y. Veksler, S. Elbaz, A. Zigelman, A. D. Gat, *Adv. Mater. Technol.* **2023**, *8*, 2202184.
[50] F. Pan, Y. Li, Z. Li, J. Yang, B. Liu, Y. Chen, *Adv. Mater.* **2019**, *31*, 1900548.
[51] O. Peretz, E. Ben Abu, A. Zigelman, S. Givli, A. D. Gat, *Nat. Commun.* **2022**, *13*, 1810.
[52] O. Peretz, E. Ben Abu, A. Zigelman, S. Givli, A. D. Gat, *Adv. Mater.* **2023**, *35*, 2301483.
[53] W. Tao, Z. Qiao, W. Zhang, in *IEEE 5th International Conference on Soft Robotics (RoboSoft)*, IEEE, New York **2022**, pp. 390–395.
[54] Y. Liu, F. Pan, B. Ding, Y. Zhu, K. Yang, Y. Chen, *Extr. Mech. Lett.* **2022**, *50*, 101535.
[55] J. Qiu, J. H. Lang, A. H. Slocum, *J. Microelectromech. Syst.* **2004**, *13*, 137.
[56] D. Melancon, A. E. Forte, L. M. Kamp, B. Gorissen, K. Bertoldi, *Adv. Funct. Mater.* **2022**, *32*, 2201891.
[57] C. Zhang, Z. Zhang, Y. Peng, Y. Zhang, S. An, Y. Wang, Z. Zhai, Y. Xu, H. Jiang, *Nat. Commun.* **2023**, *14*, 4329.


© 2024 The Author(s). Advanced Materials Technologies published by Wiley-VCH GmbH

2365709x, 2025, 4, Downloaded from https://advanced.onlinelibrary.wiley.com/doi/10.1002/admt.202401113, Wiley Online Library on [30/10/2026]. See the Terms and Conditions (https://onlinelibrary.wiley.com/terms-and-conditions) on Wiley Online Library for rules of use; OA articles are governed by the applicable Creative Commons License